Using Space Lidar Observations to Decompose Longwave Cloud Radiative Effect Variations Over the Last Decade

Thibault Vaillant de Guélis, Hélène Chepfer, Vincent Noel, Rodrigo Guzman,
David M. Winker, Riwal Plougonven

Key Points:
- Spaceborne lidar observations are useful tools to decompose the temporal variations of the cloud radiative effect into components
- In the central tropical Pacific, opaque cloud cover (47%) and temperature (33%) contribute the most to the LWCRE variations observed
- At global scale, opaque cloud cover contributes twice (58%) as much as opaque cloud temperature (28%) to the LWCRE variations observed

Using Space Lidar Observations to Decompose Longwave Cloud Radiative Effect Variations Over the Last Decade

Thibault Vaillant de Guélis[1] (iD), **Hélène Chepfer[1]** (iD), **Vincent Noel[2]** (iD), **Rodrigo Guzman[1]** (iD), **David M. Winker[3]** (iD), **and Riwal Plougonven[1]** (iD)

[1]LMD/IPSL, Sorbonne Universités, UPMC Univ Paris 06, École polytechnique, Université Paris Saclay, CNRS, Palaiseau, France, [2]Laboratoire d'Aérologie, CNRS, Toulouse, France, [3]NASA Langley Research Center, Hampton, VA, USA

Abstract Measurements of the longwave cloud radiative effect (LWCRE) at the top of the atmosphere assess the contribution of clouds to the Earth warming but do not quantify the cloud property variations that are responsible for the LWCRE variations. The CALIPSO space lidar observes directly the detailed profile of cloud, cloud opacity, and cloud cover. Here we use these observations to quantify the influence of cloud properties on the variations of the LWCRE observed between 2008 and 2015 in the tropics and at global scale. At global scale, the method proposed here gives good results except over the Southern Ocean. We find that the global LWCRE variations observed over ocean are mostly due to variations in the opaque cloud properties (82%); transparent cloud columns contributed 18%. Variation of opaque cloud cover is the first contributor to the LWCRE evolution (58%); opaque cloud temperature is the second contributor (28%).

1. Introduction

As climate warms under the influence of human activities, cloud properties (cover, profiles, and opacity) are expected to change. Multimodel analysis suggests that changes in cloud properties will contribute to enhance the cloud warming effect as climate warms, but the amplitude of the cloud feedback remains uncertain (e.g., Caldwell et al., 2016). Sorting out the contributions of cloud property variations to the top of the atmosphere (TOA) cloud radiative effect (CRE) variations is a useful step to progress in our understanding of cloud-radiation interactions in present-day climate and also to progress in our understanding of how clouds will evolve as climate warms.

Based on multimodel analysis, longwave (LW) cloud feedback is half of the total cloud feedback and intermodel spread is large (Zelinka et al., 2016). Recent model studies have successfully isolated the contributions of different cloud properties (cloud top altitude, optical depth, and total amount) to the simulated LW cloud feedback (e.g., Zelinka et al., 2012a, 2012b) using cloud radiative kernels with joint cloud top pressure and optical depth (CTP-τ) histograms from the International Satellite Cloud Climatology Project (ISCCP) (Rossow & Schiffer, 1999) simulator (Klein & Jakob, 1999). As a result, LW cloud feedback appears to strongly depend on variations in cloud vertical profile (e.g., Zelinka et al., 2012b). Moreover, variations in cloud vertical profile are expected to be a more robust signature of climate change than variations in CRE or total cloud cover because their predicted changes fall within the range of variability in the current observational record (Chepfer et al., 2014).

Observational studies trying to isolate the contributions of cloud properties to variations in LW TOA radiation are generally based on cloud radiative kernels with CTP-τ histograms from passive measurements (e.g., Norris et al., 2016; Wang & Su, 2015; Yue et al., 2016; Zhou et al., 2013). However, the essential variations in the cloud vertical profile derived from passive remote sensing are uncertain. The cloud height is inferred from cloud top temperature rather than directly measuring the height or vertical profile. When derived from active remote sensing techniques, they are much more precise and reliable because active sensors directly measure the time of flight of the photons between the emitter and the cloud (e.g., Di Michele et al., 2013; Sherwood et al., 2004; Stubenrauch et al., 2013). This is particularly true in the presence of multilayer clouds where passive retrievals are ambiguous (e.g., Holz et al., 2008). Mace and Wrenn (2013) showed that active observations give more accurate CTP-τ histograms than passive does. Kato et al. (2011) also showed that CRE is more accurate using active sensors, again mostly due to more accurate cloud heights and especially in the presence of multilayer clouds. Further, Shea et al. (2017) recently showed that uncertainties in 11 μm passive retrievals of cloud effective temperature of today's instrument (0.54–0.68 K) are 10 times greater than required to detect a

trend following the Climate Absolute Radiance and Refractivity Observatory (Wielicki et al., 2013) goal. Moreover, a long-time record with high stability is essential to study clouds and climate feedback (Wielicki et al., 2013), and current passive instruments have shown limited calibration stability over decadal timescales (e.g., Evan et al., 2007; Norris & Evan, 2015).

For a decade, satellite-borne active sensors such as the Cloud-Aerosol LIdar with Orthogonal Polarization (CALIOP; Winker et al., 2010) on board the Cloud-Aerosol Lidar and Infrared Pathfinder Satellite Observation (CALIPSO) and the Cloud Profiling Radar from CloudSat (Stephens et al., 2002) have been providing a detailed and accurate view of the cloud vertical distribution. Those observations are accurate and have the potential to stay stable over a long-time record. Indeed, lidar calibration is more stable than passive sensors because it uses the upper atmosphere as a calibration target; long-term calibration drift is near zero. However, only 10 years of records are currently available. This is not enough to study cloud changes associated to human-cause warming but is relevant to characterize covariations of cloud properties and TOA radiations in present-day climate.

In this study, we build on simplified radiative transfer model studies (Taylor et al., 2007; Yokohata et al., 2005) to propose a new method, based on spaceborne lidar observations, to partition the LWCRE variations into contributions from different cloud properties. LWCRE decomposition has already been used with the kernel method applied to lidar observations but only for cirrus clouds (Zhou et al., 2014). Here we use all lidar cloud observations with the lidar-derived LWCRE expression from Vaillant de Guélis et al. (2017) which they show is validated against the Clouds and the Earth's Radiant Energy System (CERES) measurements (see Table S1 in supporting information). Our active instrument-based framework profits from a direct measurement of altitude change, unlike the radiative kernel-based framework using cloud radiative kernels where cloud altitude change is inferred from changes in cloud amount of several bins of the CTP-τ histogram. The new framework we propose uses cloud property data for opaque clouds and thin (nonopaque) clouds, which makes sense because whether clouds are opaque or not are critical to LW radiative flux. This framework could be useful to see the impacts of changes in vertical profile of clouds to global LW feedback, especially changes that cannot be resolved in the traditional seven vertical levels in the ISCCP.

In section 2, we present a method that (i) partitions the TOA LWCRE variations into components due to cloud property variations and (ii) quantifies the fractional contribution of each cloud property to the LWCRE variations over almost a decade. In section 3, we verify the validity of the method on a well-documented El Niño event case and examine which cloud property is the main driver of the monthly mean LWCRE temporal variations between 2008 and 2015, in a tropical region and at global scale. Concluding remarks and perspectives are made in section 4.

2. Data and Methods

2.1. Observations

Guzman et al. (2017) showed that CALIOP lidar observations allow a robust and stable measurement of opaque clouds whose coverage and altitude are strongly correlated with the LWCRE. So hereafter we split the atmosphere into three atmospheric column categories: clear-sky column, opaque cloud column, and thin cloud column. In opaque cloud columns, the lidar beam is fully attenuated at the altitude of opacity Z_{Opaque}. This altitude is reached by the lidar for an optical depth τ_{VIS}, integrated from the TOA, of about 3 to 5 (Vaughan et al., 2009). This corresponds to a cloud LW emissivity of 0.8 to 0.9, considering that diffusion can be neglected in the LW domain and $\tau_{VIS}/\tau_{LW} \approx 2$ (Garnier et al., 2015). Unlike opaque clouds, thin clouds are semitransparent with optical depths smaller than 3–5, and the laser beam passes through them entirely. Note that the separation between opaque cloud columns and thin cloud columns is only made by the presence or not of Z_{Opaque}. As a consequence, optically thin cloud layers above optically opaque clouds are included in the "opaque cloud column" category.

The LWCRE is defined as the difference between clear-sky outgoing longwave radiation OLR_{Clear} and all-sky OLR_{Total}. The opaque cloud radiative effect $LWCRE_{Opaque}$ depends on the opaque cloud cover C_{Opaque}, the opaque cloud radiative temperature T_{Opaque}, average between the cloud top temperature and temperature at Z_{Opaque} using the temperature profiles of the NASA Global Modeling and Assimilation Office reanalysis (Suarez et al., 2005), and OLR_{Clear} (Vaillant de Guélis et al., 2017) (Text S1). The thin cloud radiative effect

$\text{LWCRE}_{\text{Thin}}$ depends on the thin cloud cover C_{Thin}, the thin cloud radiative temperature T_{Thin}, average between the cloud top temperature and the cloud base temperature, the thin cloud emissivity $\varepsilon_{\text{Thin}}$, and $\text{OLR}_{\text{Clear}}$. The $\text{LWCRE}_{\text{Total}}$ due to all clouds is the sum of $\text{LWCRE}_{\text{Opaque}}$ and $\text{LWCRE}_{\text{Thin}}$.

In this paper, we use 8 years (2008–2015) of monthly mean CALIPSO and CERES observations. Data collected before January 2008 are not considered because the CALIOP lidar view angle was changed from 0.3 to 3° in November 2007. Before the view angle was increased to 3°, the presence of oriented ice crystals may lead to a different relation between Z_{Opaque} and LWCRE in opaque clouds. In order to avoid all possible uncertainties due to solar noise, results presented in this paper are only for nighttime conditions. Furthermore, we restricted this study to observations over oceans to avoid uncertainties due to the ground temperature diurnal cycle over land. The gridded (2° × 2°) monthly mean cloud properties C_{Opaque}, T_{Opaque}, C_{Thin}, T_{Thin}, and $\varepsilon_{\text{Thin}}$ observations (Vaillant de Guélis et al., 2017) are derived from the GCM-Oriented CALIPSO Cloud Product (GOCCP)-OPAQ (GOCCP v3.0; Cesana & Chepfer, 2013; Chepfer et al., 2010; Guzman et al., 2017) coupled with ERA-Interim reanalysis (Dee et al., 2011). These gridded cloud properties will be publicized in the next version of GOCCP. The clear-sky $\text{OLR}_{\text{Clear}}$ observations are obtained from 1° × 1° monthly mean CERES-EBAF (Energy Balanced and Filled, edition 2.8, Loeb et al., 2009) product (made from day and night observations) that we average over 2° × 2° grid boxes. We used two different LWCRE data sets: one from the CERES-EBAF product called the "CERES-derived total LWCRE" $\text{LWCRE}_{\text{Total}}^{(\text{CERES})}$ and one called the "lidar-derived total LWCRE" $\text{LWCRE}_{\text{Total}}^{(\text{LID})}$ which is the sum of $\text{LWCRE}_{\text{Opaque}}^{(\text{LID})}$ and $\text{LWCRE}_{\text{Thin}}^{(\text{LID})}$ derived from lidar cloud observations (see next section).

2.2. Method

Using time series of spaceborne lidar and broadband radiometer measurements, we first present the method to partition the LWCRE change between two states into components due to cloud property variations. Second, we describe the method use to determine the fractional contribution for each cloud property to the LWCRE variations during the last decade.

2.2.1. Decomposing LWCRE Change Between Two States

The change in $\text{LWCRE}_{\text{Total}}^{(\text{LID})}$ ($\Delta\text{LWCRE}_{\text{Total}}^{(\text{LID})}$) between two states of the atmosphere, t_1 and t_2, can be written as follows:

$$\Delta\text{LWCRE}_{\text{Total}}^{(\text{LID})} = \Delta\text{LWCRE}_{\text{Opaque}}^{(\text{LID})} + \Delta\text{LWCRE}_{\text{Thin}}^{(\text{LID})}, \tag{1}$$

where $\Delta\text{LWCRE}_{\text{Opaque}}^{(\text{LID})}$ is the change in $\text{LWCRE}_{\text{Opaque}}^{(\text{LID})}$ between t_1 and t_2 and $\Delta\text{LWCRE}_{\text{Thin}}^{(\text{LID})}$ is the change in $\text{LWCRE}_{\text{Thin}}^{(\text{LID})}$ between t_1 and t_2.

The opaque term $\Delta\text{LWCRE}_{\text{Opaque}}^{(\text{LID})}$ can be expressed as the sum of changes due to C_{Opaque}, T_{Opaque}, $\text{OLR}_{\text{Clear}}$, and a residual nonlinear term (NL):

$$\Delta\text{LWCRE}_{\text{Opaque}}^{(\text{LID})} = \frac{\partial\text{LWCRE}_{\text{Opaque}}^{(\text{LID})}}{\partial C_{\text{Opaque}}}\Delta C_{\text{Opaque}} + \frac{\partial\text{LWCRE}_{\text{Opaque}}^{(\text{LID})}}{\partial T_{\text{Opaque}}}\Delta T_{\text{Opaque}} + \frac{\partial\text{LWCRE}_{\text{Opaque}}^{(\text{LID})}}{\partial\text{OLR}_{\text{Clear}}}\Delta\text{OLR}_{\text{Clear}}$$
$$+ \Delta\text{LWCRE}_{\text{Opaque}_{\text{NL}}}^{(\text{LID})}, \tag{2}$$

where the three partial derivatives can be obtained from the simple relationship between $\text{LWCRE}_{\text{Opaque}}^{(\text{LID})}$, C_{Opaque}, T_{Opaque}, and $\text{OLR}_{\text{Clear}}$ given in supporting information (Text S1). The residual nonlinear term cancels out ($\Delta\text{LWCRE}_{\text{Opaque}_{\text{NL}}}^{(\text{LID})} = 0$) when derivatives are computed at the mean of the two states $\frac{t_1+t_2}{2}$ (details in Text S2), as stated in Taylor et al. (2007).

Similarly, the thin term ($\Delta\text{LWCRE}_{\text{Thin}}^{(\text{LID})}$) can be expressed as follows:

$$\Delta\text{LWCRE}_{\text{Thin}}^{(\text{LID})} = \frac{\partial\text{LWCRE}_{\text{Thin}}^{(\text{LID})}}{\partial C_{\text{Thin}}}\Delta C_{\text{Thin}} + \frac{\partial\text{LWCRE}_{\text{Thin}}^{(\text{LID})}}{\partial T_{\text{Thin}}}\Delta T_{\text{Thin}} + \frac{\partial\text{LWCRE}_{\text{Thin}}^{(\text{LID})}}{\partial\varepsilon_{\text{Thin}}}\Delta\varepsilon_{\text{Thin}} + \frac{\partial\text{LWCRE}_{\text{Thin}}^{(\text{LID})}}{\partial\text{OLR}_{\text{Clear}}}\Delta\text{OLR}_{\text{Clear}}$$
$$+ \Delta\text{LWCRE}_{\text{Thin}_{\text{NL}}}^{(\text{LID})}, \tag{3}$$

where the four partial derivatives can be obtained from the simple relationship between $\text{LWCRE}_{\text{Thin}}^{(\text{LID})}$, C_{Thin}, T_{Thin}, $\varepsilon_{\text{Thin}}$, and $\text{OLR}_{\text{Clear}}$ given in supporting information (Text S1). The residual term $\Delta\text{LWCRE}_{\text{Thin}_{\text{NL}}}^{(\text{LID})}$ is quite negligible (details in Text S2). For example, when applied to the El Niño–Southern Oscillation (ENSO) case

presented in the following section, $\Delta\text{LWCRE}_{\text{Thin}_{\text{NL}}}^{\text{(LID)}}$ always represents less than 5% of $\Delta\text{LWCRE}_{\text{Thin}}^{\text{(LID)}}$ and less than 2% of $\Delta\text{LWCRE}_{\text{Total}}^{\text{(LID)}}$.

We apply equations (2) and (3) over the 8 year (2008–2015) time period: the subscript "1" refers to monthly mean value, and the subscript "2" refers to the 8 year annual mean. Doing that we obtain the partitioning of the variations of the interannual anomaly $\Delta\text{LWCRE}_{\text{Total}}^{\text{(LID)}}$ between 2008 and 2015 into contributions due to variations of the five cloud properties: C_{Opaque}, T_{Opaque}, C_{Thin}, T_{Thin}, $\varepsilon_{\text{Thin}}$, and OLR$_{\text{Clear}}$.

2.2.2. Determining the Fractional Contribution for Each Cloud Property to the LWCRE Variations During the Last Decade

To estimate which cloud properties are the main drivers of the variations in the interannual anomaly $\Delta\text{LWCRE}_{\text{Total}}^{\text{(LID)}}(t)$, we estimate the fractional contribution V_i of each cloud property $i = \{C_{\text{Opaque}}, C_{\text{Thin}}, T_{\text{Opaque}}, T_{\text{Thin}}, \varepsilon_{\text{Thin}}, (\text{OLR}_{\text{Clear}})\}$ to the variation of $\Delta\text{LWCRE}_{\text{Total}}^{\text{(LID)}}$. We apply the following equation from Boer and Yu (2003), but instead of spatial variation we consider the temporal variation:

$$V_i = \frac{\left\langle \Delta\text{LWCRE}_{\text{Total}}^{\text{(LID)}}(t)\,\Delta\text{LWCRE}_i^{\text{(LID)}}(t) \right\rangle}{\sigma^2_{\Delta\text{LWCRE}_{\text{Total}}^{\text{(LID)}}(t)}}, \tag{4}$$

where $\left\langle \Delta\text{LWCRE}_{\text{Total}}^{\text{(LID)}}(t)\,\Delta\text{LWCRE}_i^{\text{(LID)}}(t) \right\rangle$ is the covariance between the ith contributor of $\Delta\text{LWCRE}_{\text{Total}}^{\text{(LID)}}(t)$ and $\Delta\text{LWCRE}_{\text{Total}}^{\text{(LID)}}(t)$ and $\sigma^2_{\Delta\text{LWCRE}_{\text{Total}}^{\text{(LID)}}(t)}$ the temporal variance of $\Delta\text{LWCRE}_{\text{Total}}^{\text{(LID)}}(t)$. The fractional contributions sum to unity but can be negative. When negative, the contribution indicates that it reduces the variance through anticorrelation with other contributions.

3. Results

In this section, we determine which cloud property is responsible for the changes in the observed LWCRE using the method described previously. First, we focus on a well-documented case study, namely, the 2015 El Niño–Southern Oscillation event, in order to verify the validity of the method. Then, we use this same method to examine which cloud property is the main driver of the variations of $\Delta\text{LWCRE}_{\text{Total}}^{\text{(LID)}}(t)$ between 2008 and 2015.

3.1. Testing the Method on a Case Study

We apply the method described in section 2 to the 2015 October, November, December (OND) El Niño anomaly $\Delta\text{LWCRE}_{\text{Total}}^{\text{(LID)}}$, defined as the difference between the 2015 OND mean with the mean of OND months over the 2008–2015 period.

The changes of opaque and thin cloud properties (Figures S1 and S2) directly affect the LWCRE. Figure 1b shows the lidar-derived LWCRE changes inferred from these observed cloud properties. It shows consistent patterns with the LWCRE changes measured by CERES (Figure 1a). Differences in amplitude between these two figures are due to difference of sampling (full swath versus nadir) and to time of observations (night and day versus nighttime only). As a proof, Figure S4 shows how well the lidar-derived LWCRE fits with the CERES-derived LWCRE when using only nighttime measurements from CERES collocated with the CALIPSO ground track (C3M; Kato et al., 2011). We show in Figure 1 (see also 2009–2010 El Niño in Figure S3) the contribution, over the equatorial Pacific Ocean, of each of the five cloud properties to $\Delta\text{LWCRE}_{\text{Total}}^{\text{(LID)}}$ (Figure 1b). We first split $\Delta\text{LWCRE}_{\text{Total}}^{\text{(LID)}}$ into its opaque cloud contribution $\Delta\text{LWCRE}_{\text{Opaque}}^{\text{(LID)}}$ (Figure 1c) and thin cloud contribution $\Delta\text{LWCRE}_{\text{Thin}}^{\text{(LID)}}$ (Figure 1d). Then, using equations (2) and (3), we show contributions due to anomalies in opaque cloud cover and temperature (Figures 1e and 1f) and in thin cloud cover, temperature, and emissivity (Figures 1g–1i). Very significantly, we notice that $\Delta\text{LWCRE}_{\text{Total}}^{\text{(LID)}}$ (Figure 1b) is almost entirely due to the contribution of opaque clouds (Figure 1c). The strong positive anomaly of LWCRE$_{\text{Total}}^{\text{(LID)}}$ over the central tropical Pacific (160°E–160°W; 10°S–10°N) where the ascending branch of the Walker cell is located (+24 W m^{-2}) is mostly due to the increase of opaque cloud cover (+11 W m^{-2}) and the decrease of opaque cloud temperature (+9 W m^{-2}). The negative anomaly of LWCRE$_{\text{Total}}^{\text{(LID)}}$ over the western tropical Pacific
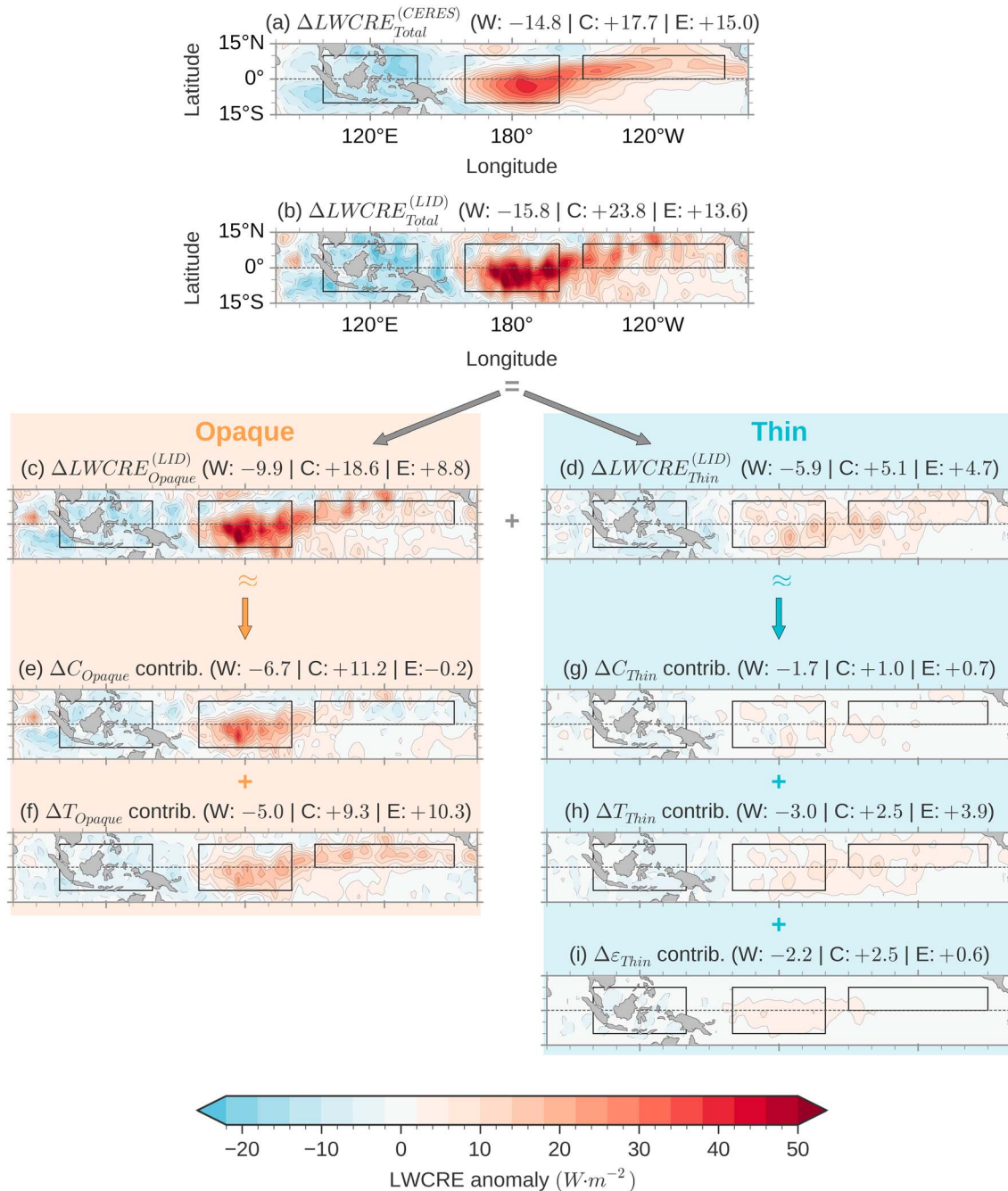
Figure 1. Partitioning of the TOA LWCRE anomaly during the 2015 El Niño into components. (a) CERES-derived LWCRE anomaly. (b) Lidar-derived LWCRE anomaly partitioned into (c) opaque LWCRE anomaly and (d) thin LWCRE anomaly, both in turn partitioned into components due to changes in (e) opaque cloud cover, (f) opaque cloud temperature, (g) thin cloud cover, (h) thin cloud temperature, and (i) thin cloud emissivity. Anomaly computed from the 2015 OND El Niño event compared to the mean of OND months on the 2008–2015 period. CERES-derived values are from CERES-EBAF Ed. 2.8 product. Lidar-derived values are only from nighttime observations. Mean values (in W m^{-2}) over the western tropical Pacific (100°E–140°E; 10°S–10°N), the central tropical Pacific (160°E–160°W; 10°S–10°N), and the eastern tropical Pacific (150°W–90°W; 0°–10°N) are given in parentheses. Sums do not match perfectly because of components due to OLR$_{Clear}$ change contribution to ΔLWCRE$_{Opaque}^{(LID)}$ (see equation (2)) (ΔOLR$_{Clear}$ contrib: (W: +1.6 | C: −1.9 | E: −1.2)) and OLR$_{Clear}$ change contribution to ΔLWCRE$_{Thin}^{(LID)}$ (see equation (4)) (ΔOLR$_{Clear}$ contrib: (W: +1.0 | C: −1.0 | E: −0.4)). Nonlinear residuals are almost negligible.

(100°E–140°E; 10°S–10°N) is also mostly due to opaque clouds for the opposite reasons. One can also notice that the positive anomaly of LWCRE$_{Total}^{(LID)}$ at the eastern part of Pacific Ocean over the equator (150°W–90°W; 0°–10°N) where Intertropical Convergence Zone reinforces (+14 W m^{-2}) is mostly due to opaque cloud temperature (+10 W m^{-2}). Indeed, in this region, opaque cloud cover remains approximately the same (Figure S1a)
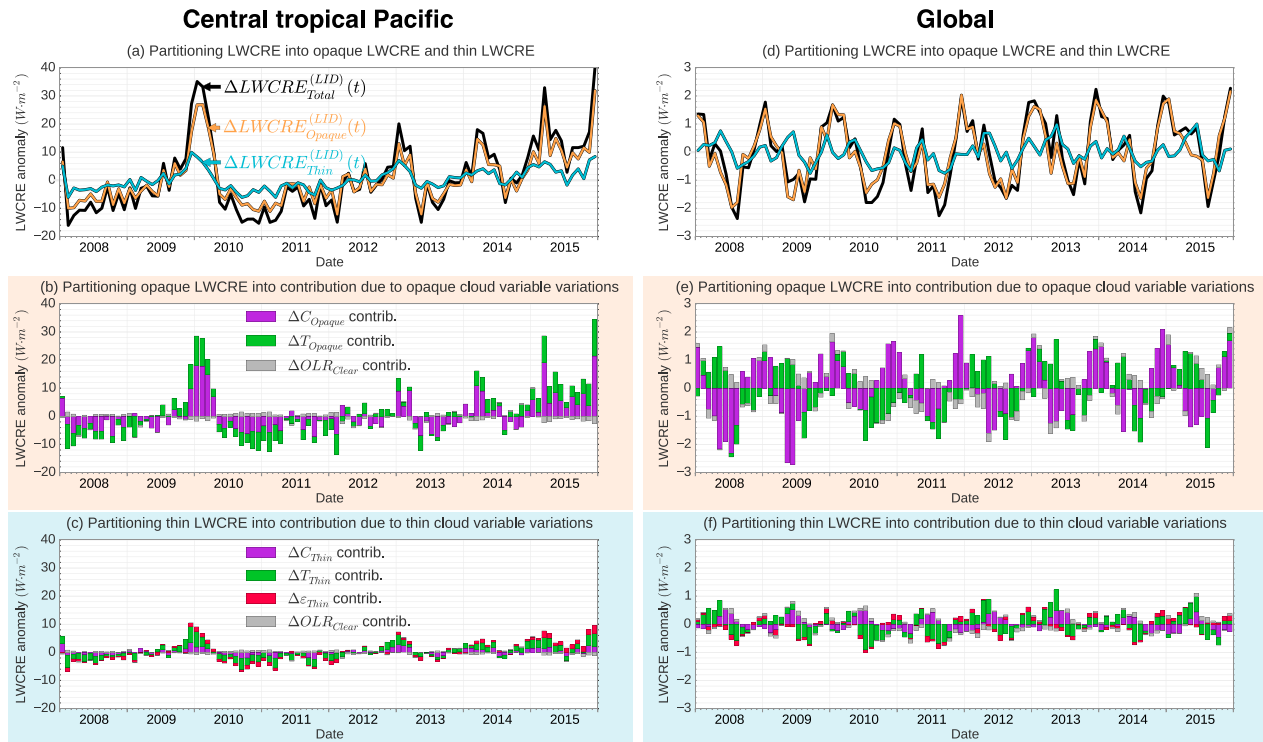
Figure 2. Partitioning of the lidar-derived TOA LWCRE time series of monthly mean anomalies between 2008 and 2015 over the central tropical Pacific region (160°E–160°W; 10°S–10°N) (left) and at global scale (right) in cloud properties contributions. (a, d) Total LWCRE partitioned in opaque cloud and thin cloud contributions, both in turn partitioned in contributions of (b, e) opaque cloud cover, opaque cloud temperature, and clear-sky properties and (c, f) thin cloud cover, thin cloud temperature, thin cloud emissivity, and clear-sky properties. Only nighttime observations over oceans are considered.

while clouds have risen to higher (colder) altitudes (Figure S1b). As the southeast part of the tropical Pacific does not show change in the vertical motion anomaly at 500 hPa (Figure S1f), cloud regime and cloud properties do not change there (Figures S1a–S1e), and the $\Delta\text{LWCRE}_{\text{Total}}^{(\text{LID})}$ is insignificant (Figure 1b). Contributions from individual cloud property changes on $\Delta\text{LWCRE}_{\text{Total}}^{(\text{LID})}$ during this El Niño event agree with previous studies using LW cloud radiative kernels derived from ISCCP joint CTP-τ histogram (Wang & Su, 2015): for example, they found, like us, that the positive LWCRE anomaly over the central tropical Pacific and the negative LWCRE anomaly over the western tropical Pacific during El Niño are approximately equal due to a change in cloud amount and cloud altitude. If our results are consistent with Wang and Su (2015) in term of pattern, signs, and variables, our study differs from Wang and Su (2015) in the amplitudes, most likely because the El Niño event analyzed is not the same (Su & Jiang, 2013). In the present study, partitioning from active lidar remote sensing can clearly separate opaque clouds and thin clouds using the atmospheric opacity measurement of Guzman et al. (2017) and provides a greater accuracy on the contribution due to cloud altitude change. This reveals the large role of opaque cloud changes in the LWCRE anomaly during an El Niño event.

3.2. Which Cloud Property Is the Main Driver of $\text{LWCRE}_{\text{Total}}^{(\text{LID})}$ Variations Between 2008 and 2015?

We now present the partitioning of the temporal variations of $\Delta\text{LWCRE}_{\text{Total}}^{(\text{LID})}(t)$ into cloud property contributions over 8 years, from January 2008 to December 2015, in the central tropical Pacific region as this region is very sensitive to the displacement of the Walker cell and so shows large LWCRE and cloud property change amplitudes (Wang & Su, 2015). After that, we examine which cloud property is the main driver of the $\Delta\text{LWCRE}_{\text{Total}}^{(\text{LID})}(t)$ variations between 2008 and 2015, in both the central Pacific region and at global scale.

Figure 2 presents time series of the monthly mean anomalies $\Delta\text{LWCRE}_{\text{Total}}^{(\text{LID})}$ partitioned into contributions due to opaque cloud property variations and thin cloud property variations over the central tropical Pacific and at
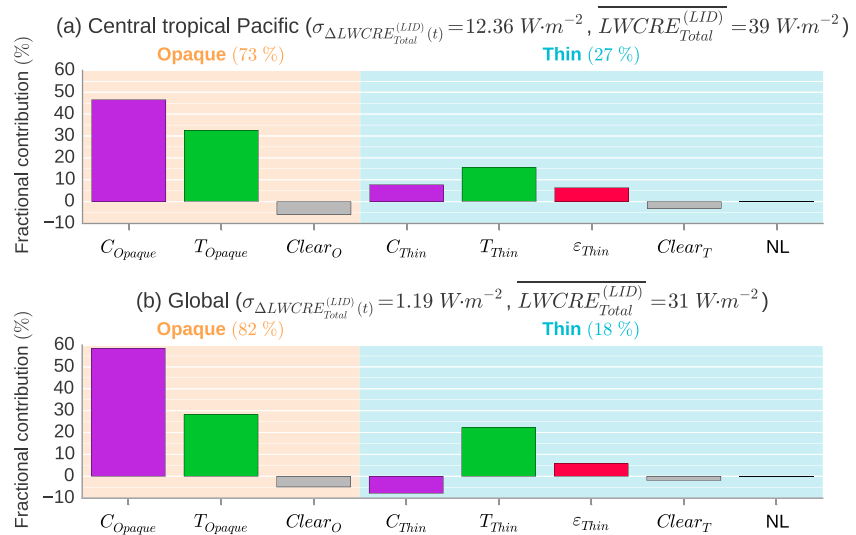
Figure 3. (a) Fractional contribution of opaque and thin cloud properties to the TOA $\text{LWCRE}_{\text{Total}}^{(\text{LID})}$ variations between 2008 and 2015. Monthly mean anomalies over the central tropical Pacific region (160°E–160°W; 10°S–10°N) for the 2008–2015 period. (b) Idem at global scale. Only nighttime observations over oceans are considered.

global scale. Temporal variations of these cloud properties are shown in Figure S5. Figure 2a shows that the lidar-derived time series $\Delta\text{LWCRE}_{\text{Total}}^{(\text{LID})}(t)$ (black line)—which correctly reproduces the CERES-derived time series $\Delta\text{LWCRE}_{\text{Total}}^{(\text{CERES})}(t)$ (Figure S5a; red line; $R = 0.97$)—is clearly driven by opaque cloud contribution time series $\Delta\text{LWCRE}_{\text{Opaque}}^{(\text{LID})}(t)$ (orange line) over the central tropical Pacific region. In this region, the amplitudes of the $\Delta\text{LWCRE}_{\text{Total}}^{(\text{LID})}(t)$ are strong because cloud cover (Figure S5b) and cloud vertical structure (Figure S5c) are very sensitive to ENSO (multivariate ENSO index, Figure S5a). As an example, the 2009–2010 El Niño event presents a strong positive $\Delta\text{LWCRE}_{\text{Total}}^{(\text{LID})}$ anomaly, due to a decrease of the opaque and thin cloud temperatures and an increase of the opaque and thin cloud coverage in this region. Figures 2b and 2c show quantitatively the contribution of these changes in opaque and thin cloud properties using the method presented in section 2.2.2. Clearly, opaque cloud cover contribution (Figure 2b, purple) drives $\Delta\text{LWCRE}_{\text{Total}}^{(\text{CERES})}(t)$ variations, followed by the opaque cloud temperature contribution (Figure 2b, green). Thin cloud property contributions (Figure 2c) do not seem to play a significant role. At global scale (Figures 2d–2f), the lidar-derived time series $\Delta\text{LWCRE}_{\text{Total}}^{(\text{LID})}(t)$ fits a little less well ($R = 0.65$) the CERES-derived $\Delta\text{LWCRE}_{\text{Total}}^{(\text{CERES})}(t)$ (Figure S5d), mainly due to errors over the Southern Ocean ($R = 0.56$; see Table S3). To drive the $\Delta\text{LWCRE}_{\text{Total}}^{(\text{LID})}(t)$ variations, contribution of a cloud property should be large and in the same way than $\Delta\text{LWCRE}_{\text{Total}}^{(\text{LID})}(t)$. It appears that opaque cloud cover contribution (Figure 2e, purple) drives $\Delta\text{LWCRE}_{\text{Total}}^{(\text{LID})}(t)$ most of the time, though opaque cloud temperature contribution (Figure 2e, green) seems to be the driver for some periods (2010 and 2015). Again, thin cloud property contributions (Figure 2f) do not seem to play a significant role, except perhaps thin cloud temperature (Figure 2f, green). We can also note that if ENSO clearly drives all the variations in central tropical Pacific (Figure S5a), it is not the case at global scale (Figure S5). There are differences in the contribution of cloud property effect to the LWCRE in the central tropical Pacific and at global scale, suggesting that the dominant mechanisms in the tropics are counteracted at the global scale by competing processes. At global scale, the $\Delta\text{LWCRE}_{\text{Total}}^{(\text{LID})}(t)$ variations do not seem to be driven by a specific region. Splitting global ocean into tropics (30°S–30°N) and midlatitudes (30°–65°) shows that the $\Delta\text{LWCRE}_{\text{Total}}^{(\text{LID})}(t)$ variations in both regions track the global scale $\Delta\text{LWCRE}_{\text{Total}}^{(\text{LID})}(t)$ variations (Figure S6).

Using equation (4), we can attribute for each component its fractional contribution to the $\Delta\text{LWCRE}_{\text{Total}}^{(\text{LID})}(t)$ variations between 2008 and 2015. This lets us organize the different contributions into a hierarchy and

emphasize the main drivers responsible for the $\Delta\text{LWCRE}_{\text{Total}}^{(\text{LID})}(t)$ variations. Figure 3a shows the fractional contributions of each components. Clearly, changes in opaque cloud properties drive (73%) the $\Delta\text{LWCRE}_{\text{Total}}^{(\text{LID})}(t)$ variations between 2008 and 2015 over the central tropical Pacific region. Changes in C_{Opaque} contribute the most (47%), followed by changes in T_{Opaque} (33%). The weak negative contribution from clear-sky (-6% for Clear$_O$) is due to the fact that changes in OLR$_{\text{Clear}}$ tend to diminish the $\Delta\text{LWCRE}_{\text{Total}}^{(\text{LID})}(t)$ anomaly caused by cloud changes. Indeed, warm phases of ENSO correspond to a strong positive anomaly of $\Delta\text{LWCRE}_{\text{Total}}^{(\text{LID})}(t)$, due to cloud property anomalies, which is slightly diminished by the decrease in OLR$_{\text{Clear}}$ due to an increase of the humidity in this region.

Figure 3b shows the same fractional contributions but at global scale. Again, opaque clouds seem to largely drive the $\Delta\text{LWCRE}_{\text{Total}}^{(\text{LID})}(t)$ variations between 2008 and 2015 (82%), albeit the opaque cloud cover only represents half of the global mean total cloud cover over the entire Earth oceans (Vaillant de Guélis et al., 2017). Opaque cloud cover appears to play the major role (58%), certainly mainly because of strong variations of opaque cloud cover in the midlatitude regions (see Table S2). Opaque cloud temperature plays a less important role (28%). Finally, thin clouds make a small contribution, mostly due to changes in cloud temperature (22%). Though opaque clouds contribute much more to $\Delta\text{LWCRE}_{\text{Total}}^{(\text{LID})}(t)$ than thin clouds, the LWCRE of high opaque cloud cover changes is largely canceled by their SWCRE (Loeb et al., 2009; Zelinka et al., 2012a). As a result, the opaque cloud cover changes may not contribute too much to net CRE. Even though our approach lets us quantify the roles played by different cloud properties, the results at global scale need to be looked with caution as the $\Delta\text{LWCRE}_{\text{Total}}^{(\text{LID})}(t)$ temporal variations at this scale fit less well with CERES observations than over central tropical Pacific region.

4. Conclusions

This paper presents a method that uses, for the first time, observations collected by lidar onboard satellite to decompose the interannual variations of the monthly mean LWCRE anomaly into contributions due to changes in five cloud properties: opaque cloud cover, opaque cloud temperature, thin cloud cover, thin cloud temperature, and thin cloud emissivity. We apply this method to the CALIPSO 2008–2015 record and find the following results:

1. In the central tropical Pacific (Figure 3a), 73% of LWCRE interannual variations observed between 2008 and 2015 are due to changes in opaque clouds; the other 27% are due to changes in thin clouds. The two opaque cloud properties—opaque cloud cover and opaque cloud temperature—strongly contribute to LWCRE interannual variations (respectively 47% and 33%).
2. At global scale (Figure 3b), the LWCRE interannual variations observed during the 2008–2015 period are also mostly (82%) driven by changes in opaque clouds while thin clouds only contribute 18%. LWCRE interannual variations are more influenced by changes in the opaque cloud cover (58%) than changes in the opaque cloud temperature (28%).

Our results highlight the important radiative role played by opaque clouds: representing half of the global mean total cloud cover over the oceans, they are responsible for 82% of the global monthly mean LWCRE interannual variations. These results also underline the usefulness of spaceborne lidar observations to better understand LWCRE changes. Due to their accuracy and stability over time, a multidecade lidar-in-space record, analyzed as in the current paper, can provide observational constraints on LW cloud feedbacks. CALIOP over the last decade, the upcoming spaceborne lidar from EarthCARE (Illingworth et al., 2015) to be launched in 2019, and hopefully a third lidar afterward, may allow construction of a sufficiently long spaceborne lidar record. Meanwhile, it is planned to implement the cloud properties used in this method into the CFMIP Observation Simulator Package (Bodas-Salcedo et al., 2011) lidar simulator (Cesana & Chepfer, 2012; Chepfer et al., 2008; Guzman et al., 2017). With these new simulator outputs, we plan to study how climate models simulate the interannual covariations of cloud properties and the LWCRE and compute the internal variability cloud feedback, the so-called "short-term" cloud feedback (Dessler, 2010, 2013), in climate models that we could compare to the short-term cloud feedback in observations.

References

Bodas-Salcedo, A., Webb, M. J., Bony, S., Chepfer, H., Dufresne, J. L., Klein, S. A., … John, V. O. (2011). COSP: Satellite simulation software for model assessment. *Bulletin of the American Meteorological Society*, *92*(8), 1023. https://doi.org/10.1175/2011BAMS2856.1

Boer, G., & Yu, B. (2003). Climate sensitivity and response. *Climate Dynamics*, *20*(4), 415–429. https://doi.org/10.1007/s00382-002-0283-3

Caldwell, P. M., Zelinka, M. D., Taylor, K. E., & Marvel, K. (2016). Quantifying the sources of intermodel spread in equilibrium climate sensitivity. *Journal of Climate*, *29*(2), 513–524. https://doi.org/10.1175/JCLI-D-15-0352.1

Cesana, G., & Chepfer, H. (2012). How well do climate models simulate cloud vertical structure? A comparison between CALIPSO-GOCCP satellite observations and CMIP5 models. *Geophysical Research Letters*, *39*, L20803. https://doi.org/10.1029/2012GL053153

Cesana, G., & Chepfer, H. (2013). Evaluation of the cloud thermodynamic phase in a climate model using CALIPSO-GOCCP. *Journal of Geophysical Research: Atmospheres*, *118*, 7922–7937. https://doi.org/10.1002/jgrd.50376

Chepfer, H., Bony, S., Winker, D., Cesana, G., Dufresne, J. L., Minnis, P., … Zeng, S. (2010). The GCM-oriented CALIPSO cloud product (CALIPSO-GOCCP). *Journal of Geophysical Research*, *115*, D00H16. https://doi.org/10.1029/2009JD012251

Chepfer, H., Bony, S., Winker, D., Chiriaco, M., Dufresne, J.-L., & Sèze, G. (2008). Use of CALIPSO lidar observations to evaluate the cloudiness simulated by a climate model. *Geophysical Research Letters*, *35*, L15704. https://doi.org/10.1029/2008GL034207

Chepfer, H., Noel, V., Winker, D., & Chiriaco, M. (2014). Where and when will we observe cloud changes due to climate warming? *Geophysical Research Letters*, *41*, 8387–8395. https://doi.org/10.1002/2014GL061792

Dee, D. P., Uppala, S. M., Simmons, A. J., Berrisford, P., Poli, P., Kobayashi, S., … Vitart, F. (2011). The ERA-Interim reanalysis: Configuration and performance of the data assimilation system. *Quarterly Journal of the Royal Meteorological Society*, *137*(656), 553–597. https://doi.org/10.1002/qj.828

Dessler, A. E. (2010). A determination of the cloud feedback from climate variations over the past decade. *Science*, *330*(6010), 1523–1527. https://doi.org/10.1126/science.1192546

Dessler, A. E. (2013). Observations of climate feedbacks over 2000–10 and comparisons to climate models. *Journal of Climate*, *26*(1), 333–342. https://doi.org/10.1175/JCLI-D-11-00640.1

Evan, A. T., Heidinger, A. K., & Vimont, D. J. (2007). Arguments against a physical long-term trend in global ISCCP cloud amounts. *Geophysical Research Letters*, *34*, L04701. https://doi.org/10.1029/2006GL028083

Garnier, A., Pelon, J., Vaughan, M. A., Winker, D. M., Trepte, C. R., & Dubuisson, P. (2015). Lidar multiple scattering factors inferred from CALIPSO lidar and IIR retrievals of semi-transparent cirrus cloud optical depths over oceans. *Atmospheric Measurement Techniques*, *8*(7), 2759–2774. https://doi.org/10.5194/amt-8-2759-2015

Guzman, R., Chepfer, H., Noel, V., Vaillant de Guélis, T., Kay, J. E., Raberanto, P., … Winker, D. M. (2017). Direct atmosphere opacity observations from CALIPSO provide new constraints on cloud-radiation interactions. *Journal of Geophysical Research: Atmospheres*, *122*, 1066–1085. https://doi.org/10.1002/2016JD025946

Holz, R. E., Ackerman, S. A., Nagle, F. W., Frey, R., Dutcher, S., Kuehn, R. E., … Baum, B. (2008). Global Moderate Resolution Imaging Spectroradiometer (MODIS) cloud detection and height evaluation using CALIOP. *Journal of Geophysical Research*, *113*, D00A19. https://doi.org/10.1029/2008JD009837

Illingworth, A. J., Barker, H. W., Beljaars, A., Ceccaldi, M., Chepfer, H., Clerbaux, N., … van Zadelhoff, G.-J. (2015). The EarthCARE satellite: The next step forward in global measurements of clouds, aerosols, precipitation, and radiation. *Bulletin of the American Meteorological Society*, *96*(8), 1311–1332. https://doi.org/10.1175/BAMS-D-12-00227.1

Kato, S., Rose, F. G., Sun-Mack, S., Miller, W. F., Chen, Y., Rutan, D. A., … Collins, W. D. (2011). Improvements of top-of-atmosphere and surface irradiance computations with CALIPSO-, CloudSat-, and MODIS-derived cloud and aerosol properties. *Journal of Geophysical Research*, *116*, D19209. https://doi.org/10.1029/2011JD016050

Klein, S. A., & Jakob, C. (1999). Validation and sensitivities of frontal clouds simulated by the ECMWF model. *Monthly Weather Review*, *127*(10), 2514–2531. https://doi.org/10.1175/1520-0493(1999)127%3C2514:VASOFC%3E2.0.CO;2

Loeb, N. G., Wielicki, B. A., Doelling, D. R., Smith, G. L., Keyes, D. F., Kato, S., … Wong, T. (2009). Toward optimal closure of the Earth's top-of-atmosphere radiation budget. *Journal of Climate*, *22*(3), 748–766. https://doi.org/10.1175/2008JCLI2637.1

Mace, G. G., & Wrenn, F. J. (2013). Evaluation of the hydrometeor layers in the east and west Pacific within ISCCP Cloud-top pressure–optical depth bins using merged *CloudSat* and *CALIPSO* data. *Journal of Climate*, *26*(23), 9429–9444. https://doi.org/10.1175/JCLI-D-12-00207.1

Di Michele, S., McNally, T., Bauer, P., & Genkova, I. (2013). Quality assessment of cloud-top height estimates from satellite IR radiances using the CALIPSO lidar. *IEEE Transactions on Geoscience and Remote Sensing*, *51*(4), 2454–2464. https://doi.org/10.1109/TGRS.2012.2210721

Norris, J. R., Allen, R. J., Evan, A. T., Zelinka, M. D., O'Dell, C. W., & Klein, S. A. (2016). Evidence for climate change in the satellite cloud record. *Nature*, *536*, 72–75. https://doi.org/10.1038/nature18273

Norris, J. R., & Evan, A. T. (2015). Empirical removal of artifacts from the ISCCP and PATMOS-x satellite cloud records. *Journal of Atmospheric and Oceanic Technology*, *32*(4), 691–702. https://doi.org/10.1175/JTECH-D-14-00058.1

Rossow, W. B., & Schiffer, R. A. (1999). Advances in understanding clouds from ISCCP. *Bulletin of the American Meteorological Society*, *80*(11), 2261–2287. https://doi.org/10.1175/1520-0477(1999)080%3C2261:AIUCFI%3E2.0.CO;2

Shea, Y. L., Wielicki, B. A., Sun-Mack, S., & Minnis, P. (2017). Quantifying the dependence of satellite cloud retrievals on instrument uncertainty. *Journal of Climate*. https://doi.org/10.1175/JCLI-D-16-0429.1

Sherwood, S. C., Chae, J.-H., Minnis, P., & McGill, M. (2004). Underestimation of deep convective cloud tops by thermal imagery. *Geophysical Research Letters*, *31*, L11102. https://doi.org/10.1029/2004GL019699

Stephens, G. L., Vane, D. G., Boain, R. J., Mace, G. G., Sassen, K., Wang, Z., … The CloudSat Science Team (2002). The CloudSat mission and the A-Train: A new dimension of space-based observations of clouds and precipitation. *Bulletin of the American Meteorological Society*, *83*(12), 1771–1790. https://doi.org/10.1175/BAMS-83-12-1771

Stubenrauch, C. J., Rossow, W. B., Kinne, S., Ackerman, S., Cesana, G., Chepfer, H., … Zhao, G. (2013). Assessment of global cloud datasets from satellites: Project and database initiated by the GEWEX radiation panel. *Bulletin of the American Meteorological Society*, *94*(7), 1031–1049. https://doi.org/10.1175/BAMS-D-12-00117.1

Su, H., & Jiang, J. H. (2013). Tropical clouds and circulation changes during the 2006/07 and 2009/10 El Niños. *Journal of Climate*, *26*(2), 399–413. https://doi.org/10.1175/JCLI-D-12-00152.1

Suarez, M. J., Bloom, S., da Silva, A., Dee, D., Bosilovich, M., Chern, J.-D., … Wu, M.-L. (2005). Documentation and validation of the Goddard Earth Observing System (GEOS) data assimilation system, version 4.

Taylor, K. E., Crucifix, M., Braconnot, P., Hewitt, C. D., Doutriaux, C., Broccoli, A. J., … Webb, M. J. (2007). Estimating shortwave radiative forcing and response in climate models. *Journal of Climate*, *20*(11), 2530–2543. https://doi.org/10.1175/JCLI4143.1

Vaillant de Guélis, T., Chepfer, H., Noel, V., Guzman, R., Dubuisson, P., Winker, D. M., & Kato, S. (2017). Link between the outgoing longwave radiation and the altitude where the space-borne lidar beam is fully attenuated. *Atmospheric Measurement Techniques Discussions*. in review, https://doi.org/10.5194/amt-2017-115

Vaughan, M. A., Powell, K. A., Winker, D. M., Hostetler, C. A., Kuehn, R. E., Hunt, W. H., … McGill, M. J. (2009). Fully automated detection of cloud and aerosol layers in the CALIPSO lidar measurements. *Journal of Atmospheric and Oceanic Technology*, *26*(10), 2034–2050. https://doi.org/10.1175/2009JTECHA1228.1

Wang, H., & Su, W. (2015). The ENSO effects on tropical clouds and top-of-atmosphere cloud radiative effects in CMIP5 models. *Journal of Geophysical Research: Atmospheres*, *120*, 4443–4465. https://doi.org/10.1002/2014JD022337

Wielicki, B. A., Young, D. F., Mlynczak, M. G., Thome, K. J., Leroy, S., Corliss, J., … Xiong, X. (2013). Achieving climate change absolute accuracy in orbit. *Bulletin of the American Meteorological Society*, *94*(10), 1519–1539. https://doi.org/10.1175/BAMS-D-12-00149.1

Winker, D. M., Pelon, J., Coakley, J. A. Jr., Ackerman, S. A., Charlson, R. J., Colarco, P. R., … Wielicki, B. A. (2010). The CALIPSO mission: A global 3D view of aerosols and clouds. *Bulletin of the American Meteorological Society*, *91*(9), 1211–1229. https://doi.org/10.1175/2010BAMS3009.1

Yokohata, T., Emori, S., Nozawa, T., Tsushima, Y., Ogura, T., & Kimoto, M. (2005). A simple scheme for climate feedback analysis. *Geophysical Research Letters*, *32*, L19703. https://doi.org/10.1029/2005GL023673

Yue, Q., Kahn, B. H., Fetzer, E. J., Schreier, M., Wong, S., Chen, X., & Huang, X. (2016). Observation-based longwave cloud radiative kernels derived from the A-train. *Journal of Climate*, *29*(6), 2023–2040. https://doi.org/10.1175/JCLI-D-15-0257.1

Zelinka, M. D., Klein, S. A., & Hartmann, D. L. (2012a). Computing and partitioning cloud feedbacks using cloud property histograms. Part I: Cloud radiative kernels. *Journal of Climate*, *25*(11), 3715–3735. https://doi.org/10.1175/JCLI-D-11-00248.1

Zelinka, M. D., Klein, S. A., & Hartmann, D. L. (2012b). Computing and partitioning cloud feedbacks using cloud property histograms. Part II: Attribution to changes in cloud amount, altitude, and optical depth. *Journal of Climate*, *25*(11), 3736–3754.

Zelinka, M. D., Zhou, C., & Klein, S. A. (2016). Insights from a refined decomposition of cloud feedbacks. *Geophysical Research Letters*, *43*, 9259–9269. https://doi.org/10.1002/2016GL069917

Zhou, C., Dessler, A. E., Zelinka, M. D., Yang, P., & Wang, T. (2014). Cirrus feedback on inter-annual climate fluctuations. *Geophysical Research Letters*, *41*, 9166–9173. https://doi.org/10.1002/2014GL062095

Zhou, C., Zelinka, M. D., Dessler, A. E., & Yang, P. (2013). An analysis of the short-term cloud feedback using MODIS data. *Journal of Climate*, *26*(13), 4803–4815. https://doi.org/10.1175/JCLI-D-12-00547.1